SEI Formation Mechanisms and Li^+ Dissolution in Lithium Metal Anodes: Impact of the Electrolyte Composition and the Electrolyte-to-Anode Ratio

Saul Perez Beltran[1], and Perla B. Balbuena[1,2,3],*

[1]Department of Chemical Engineering, [2]Department of Materials Science and Engineering, and

[3]Department of Chemistry, Texas A&M University, College Station, Texas 77843, United States

*e-mail: balbuena@tamu.edu

Abstract

The lithium metal battery is one of today's most promising high-energy-density storage devices. Its full-scale implementation depends on solving operational and safety issues intrinsic to the Li metal high reactivity leading to uncontrolled electrolyte decomposition and uneven Li deposition. In this work, we study the spontaneous formation of the solid electrolyte interphase (SEI) upon contact of Li metal with the electrolyte and describe the heterogeneous SEI morphological features. Multiple electrolyte formulations based on lithium bis(fluorosulfonyl)imide (LiFSI), dimethoxyethane (DME), dimethyl carbonate (DMC), 1,2,2-tetrafluoroethyl-2,2,3,3-tetrafluoropropyl ether (TTE) and bis(2,2,2-trifluoroethyl) ether (BTFE) are used. Findings include the description of the SEI evolution from dispersed LiO, LiS, LiN, and LiF clusters to a continuous and compact inorganic phase in which the LiO and LiF content depend on the presence of fluorine diluents. The role of the DME ether solvent helping the growth of a "wet-SEI" is compared to that of the highly unstable carbonate DMC, which decomposes into complex radical oligomers that might contribute to further electrolyte decomposition. The impact of the electrolyte-to-anode ratio on LiFSI decomposition is highlighted. Finally, we suggest the existence of a critical LiFSI concentration and electrolyte-to-anode ratio that could potentially balance the rate of electrolyte depletion and lithium consumption.

Keywords: ab initio molecular dynamics, classical molecular dynamics, SEI composition and morphology, interfacial reactions

Introduction

Society's ever-increasing energy demand, tied with depleting oil reserves and growing environmental issues, pushes for the constant development of clean energy production strategies and innovative energy storage devices. In this regard, lithium metal batteries (LMBs) based on high-voltage cathodes are among the most promising high-energy-density storage devices that can usher in the full-scale electrification of the transportation sector and the build-up of a robust grid energy storage network.[1-4] Lithium metal is lightweight and offers a very high theoretical capacity (3860 mAh/g vs. graphite's 372 mhA/g).[5-7] However, its successful introduction as an anode material relies on solving intrinsic operational and safety issues related to its high reactivity, uncontrolled electrolyte decomposition, and uneven and dendritic lithium deposition.[7]

The strategies for stabilizing the lithium metal pass through introducing either solid electrolytes or highly concentrated liquid formulations,[8, 9] the introduction of copper or graphene-based lithium hosts,[10, 11] and even use of high-pressure operation conditions,[12] among others.[13, 14] However, regardless of the significant improvements over the past few years,[14] most battery assemblies suffer a sudden capacity drop after reaching a certain percentage of the original cell capacity,[15, 16] and the cause for this odd behavior is yet due for complete elucidation. So far, the understanding is that the lithium metal anode lifespan depends on the interfacial dynamics with the electrolyte; both the lithium metal and the electrolyte get consumed during cycling, and the battery dies off whenever either one depletes.[15, 17] The viable way then seems to figure out how to slow down enough both the electrolyte degradation and the lithium metal loss to enable a battery stability sufficiently high to meet the minimum operational needs, a very challenging task, as reaching the >99.9% Coulombic efficiency (CE) goal set by the

Department of energy is yet unmet even though the overwhelming research work devoted to understanding the lithium/electrolyte interface dynamics.[14, 18]

Since the discovery of the solid-electrolyte interphase (SEI),[19] it has become clear that it plays a major role in the battery degradation phenomena. However, the SEI morphology, growth, and composition are constantly debated. This work narrows down the understanding gap of the lithium metal/electrolyte interfacial dynamics via a computational approach introduced recently that solves the time window limitation problem of the ab initio molecular dynamics method (AIMD) by performing the calculation through a hybrid ab initio and reactive force field (ReaxFF) sequence (HAIR) to extend the simulation to hundreds to picoseconds without losing access to the AIMD accuracy.[20-22] We model the spontaneous formation of the SEI on a lithium metal surface using different electrolyte formulations and electrolyte-to-anode ratios. We work with low concentration and high concentration electrolytes (HCE)[8] based on lithium bis(fluorosulfonyl)imide (LiFSI) in two solvents such as dimethoxyethane (DME) and dimethyl carbonate (DMC). We also include multiple localized high concentration electrolyte (LHCE)[8] formulations by testing two fluorinated diluents such as 1,2,2-tetrafluoroethyl-2,2,3,3-tetrafluoropropyl ether (TTE) and bis(2,2,2-trifluoroethyl) ether (BTFE). In most cases, the simulation results are compared to available experimental information.

Materials and Methods

Simulation Approach

We performed our calculations following the HAIR simulation scheme recently introduced to model the reductive decomposition reaction of lithium bis(trifluoromethanesulfonyl)imide salts (LiTFSI) and 1,3-dioxolane (DOL) solvent molecules on a lithium metal surface.[20, 21] The HAIR scheme uses the ab-initio molecular dynamics (AIMD) and the reactive force field (ReaxFF) methods in sequence to provide a more accurate calculation than a purely classical molecular dynamics method while extending the achievable simulation time to hundreds of picoseconds (ps). The calculation of ground-state energy

precedes every molecular dynamic step, and classical mechanics defines the ionic trajectories depending on the specificities of either method (AIMD and ReaxFF). The AIMD intervals address the localized interfacial electrochemical reactions, while the ReaxFF gives access to long-range mass transfer processes (longer-time chemical reactions in the electrolyte).

The AIMD calculations are implemented with the Vienna ab initio simulation package (VASP, version 5.4.4).[23-26] The approximation of the exchange-correlation energy is with the Perdew-Burke-Ernzerhof (PBE) functional, while the projector augmented wave (PAW) method describes valence electrons with a plane-wave basis expansion up to 400 eV. [27, 28] Furthermore, the Monkhorst-Pack scheme samples the Brillouin zone with a 1x1x1 grid density,[29] and the Gaussian smearing method set to 0.05 eV deals with partial occupancies. Finally, the convergence criteria for the electronic self-consistent is 10^{-4} eV. The AIMD calculation step is with the NVT ensemble set at 300 K, runs for 0.5 ps, and uses a 1.2 fs time-step; this relatively long time-step comes only after increasing the hydrogen mass to its tritium isotope.[30] The Nose-Hoover thermostat is set to 0.5 to control the temperature, and Newton's equations are integrated with the Verlet algorithm.

The ReaxFF step runs with the large-scale atomic/molecular massively parallel simulation software (LAMMPS, version 3Mar20).[31] The ReaxFF parameterization is specifically updated to describe FSI^- anions and organic solvents interfacing with lithium surfaces.[21] The ReaxFF MD run is with the NVT ensemble for about five ps with a 0.25 fs time-step and time integration with the Nose-Hoover method with the damping parameter set to 0.01 fs^{-1}. Each HAIR cycle has an AIMD step followed by a ReaxFF calculation, and we executed about 46 cycles in each case to complete a simulation window 253 ps long.

Both HCE and LHCE electrolytes display three-dimensional aggregated structures formed due to increased ionic association because of the high lithium salt content.[32-34] We allow these aggregated structures to develop in our simulation cells by running a preliminary ReaxFF calculation for about 50 ps with the lithium slab atomic positions fixed, and all lithium and electrolyte atomic charges fixed to their equivalent vacuum electronic distribution. The 253 ps simulation window mentioned above comes after

this preliminary calculation. Fixing the atomic slab positions and freezing all the electronic charges makes the lithium slab inert and allows for the formation of solvation structures within the electrolyte, hindering the reactivity at the electrolyte/slab interface before applying the HAIR scheme.

We do not model the voltage discharge explicitly as we do not apply an electric bias nor change the number of electrons to achieve an specified electron chemical potential at the electrode/electrolyte interface.[35, 36] However, our simulations provide information electrochemical reactions driven by instantaneous and localized voltage changes and provide valuable insights into the electrode/electrolyte interface's reaction mechanisms.[37]

Simulation cell

The simulation cell is a tetragonal array with dimensions 13.78 Å x 13.78 Å x 39.21 Å along the x-, y-, and z- coordinates. Periodic boundary conditions apply throughout the x- and y-coordinates while a He-atom layer along the x-y plane breaks the periodicity along the z-coordinate. Figure 1 shows the initial configuration for a LiFSI:DME (1:16 molar ratio) facing a thirteen-layer lithium slab cut along the (100) surface; earlier works identified this crystal facet as the most stable (lowest energy) lithium surface.[38, 39] The Li slab thickness is Z_A, while Z_E represents the z-component of the space available for the electrolyte molecules; the Z_E/Z_A fraction defines the electrolyte to anode ratio.

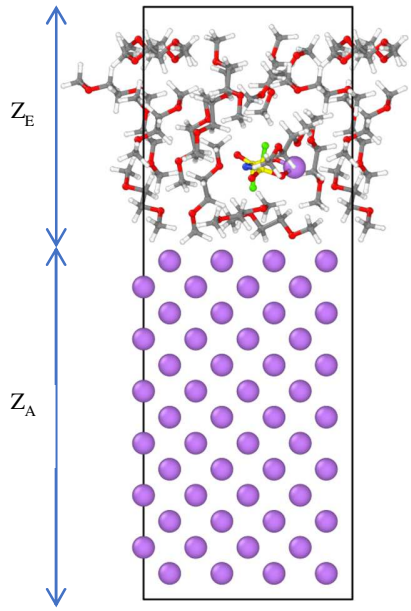

Figure 1: Initial configuration simulation cell LiFSI:DME (E-1) || Li(100). Li atoms in purple, S in yellow, O in red, N in blue, F in green, C in gray, and H in white. Not showing the bottom He atom layer along the x-y plane.

Table 1 lists the electrolyte formulations studied here, their molarities, molar ratios and densities, and references to experimental works. The insertion of the electrolyte molecules into the simulation cell is with the so-called "Amorphous Cell" built-in packing tool available in the Biovia Materials Studio software (MS - version 8.0).[40]

Table 1: Electrolyte Formulations studied in this work. The (*) symbol highlights the estimated parameters needed for the packing procedure in MS.

Electrolyte formulation	Label	Molarity [M] / References	Molar ratio	Density [g/cm^3]
LiFSI:DME	E-1	1 [41]	1:16	0.87
	E-2	3.7 [42]	1:2.2	1.37
	E-3	4.4 [42]	1:1.3	1.40
	E-4	10 *	8:1	1.8*
LiFSI:DMC	C-1	0.91 [43]	1:19	1.20
	C-2	4.6 [43]	9:16	1.50
	C-3	10 *	16:6	1.8*

LiFSI:DME/TTE	ET-1	1.52 [15, 42]	1:1.5:3.5	1.57
LiFSI:DME/BTFE	EB-1	1.65 [44]	1:1.0:2.67	1.40
LiFSI:DMC/TTE	CT-1	1.35 [43]	1:1.5:8	1.55
LiFSI:DMC/BTFE	CB-1	2.52 [8]	1:1.5:1.5	1.48

Results

Low Concentration vs. High Concentration Electrolytes

Figure 2(a) shows the initial configuration for the 1 M E-1 electrolyte facing the Li(100) surface at a 0.75 Z_E/Z_A ratio. The FSI^- anion decomposition is spontaneous and starts with a defluorination process and an S-O bond cleavage within the first 5.5 ps to produce LiF and LiO complexes together with NSO^{2-} and SO_2F^- fragments (Figure 2(b)). This decomposition path agrees with earlier theoretical studies with a 1 M LiFSI/1,3-dioxolane (DOL) electrolyte where the defluorination and later S-N cleavage are the initiating steps for the FSI^- decomposition.[21] The anion decomposition completes before 11 ps to form multiple complexes such as LiO, LiS, LiF and LiN. However, the low salt concentration makes these complexes dispersed, and a continuous inorganic SEI phase does not form. Regarding the organic SEI phase, the DME solvent resists the lithium metal dissolution, with only one DME molecule reducing into two O-CH_3^- fragments and a CH_2-CH_2 molecule (Figure 2(d)). One O-CH_3^- radical further decomposes into O-CH^-_2 leading to the formation of a LiH complex. The lithium metal completely dissolves into Li^+ ions, and no further DME reduction happens after 253 ps (Figure 2(e)). X-ray photoelectron spectroscopy (XPS) measurements performed on an SEI spontaneously formed on a lithium metal foil soaked in a 1 M LiFSI:DME electrolyte suggests the formation of LiF and LiN.[41] Further elemental composition analyses of these samples indicate the formation of lithium alkyl carbonate ($ROCO_2Li$), lithium alkyl oxide (ROLi) structures and other organic groups (C-OR and C-C/C-H), once again in qualitative agreement with our calculation. The formation of LiH in the SEI is controversial because of its instability against moisture and an x-ray diffraction (XRD) pattern similar to LiF.[45] Still, it has been detected recently with in-situ synchrotron-based X-ray diffraction measurements (XRD) and pair distribution function analyses performed on a cycled lithium metal anode.[45]

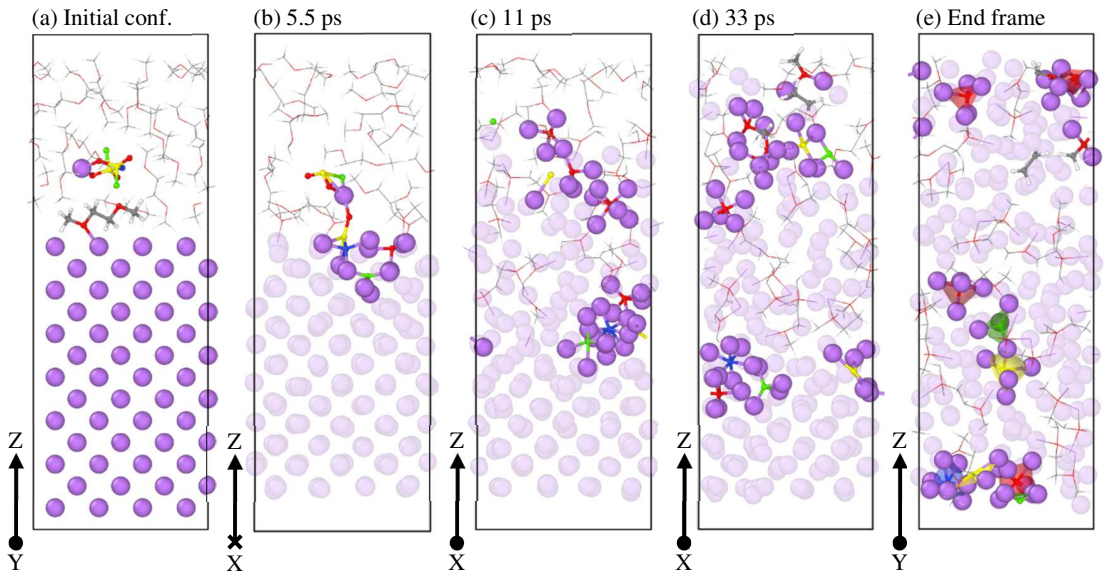

Figure 2: Selected frames from the simulation with 1M E-1 electrolyte at a 0.75 Z_E/Z_A ratio. The atom colors are the same as in Figure 1. The red polyhedra correspond to LiO complexes, the green to LiF complexes, and the blue and yellow ones to LiN and LiS

Figure 3(a) plots the SEI formation process throughout the calculation with the 3.7 M E-2 electrolyte by counting the number of each species present throughout the simulation. The initial eleven DME molecules survive to the end while the FSI^- anions quickly decompose to grow the inorganic SEI. This finding agrees with ealier XPS measurements of a LiFSI:DME-derived SEI (1:1.2 molar ratio), suggesting that the SEI layer on lithium metal derives mainly from FSI^- anions.[42] The end frame at 253 ps in Figure 3(b) shows no lithium metal left and displays the morphological features of the resulting SEI. The inorganic SEI grows into multiple and extended amorphous domains propelled by the high FSI^- concentration, and the polyhedral visualization of this inorganic SEI shows multiple and segregated phases of LiO (red polyhedra), LiF (green), LiS (yellow), and LiN (blue). The presence of LiN confirms complete FSI^- decomposition, in agreement with XPS measurements performed on LiFSI:DME-derived SEIs (1:1.2 molar ratio) on lithium metal.[41, 42]

The relative content of each phase depends on the availability of oxygen, fluorine, sulfur, and nitrogen species released after the FSI^- decomposition. These inorganic domains are mediated by Li^+ ions

dissolved in the DME solvent. This morphology resembles the so-called "wet SEI," where the electrolyte wets the inorganic SEI and helps the dissolved Li^+ ions diffuse back and forth to continue the electrochemical reactions.[15] The positive impact of this "wet SEI" correlates with scanning electron microscopy (SEM) imaging performed on electrodeposited lithium metal films with LiFSI:DME (1:1.2) that show uniform and denser films that suggest improved lithium metal stability.[42]

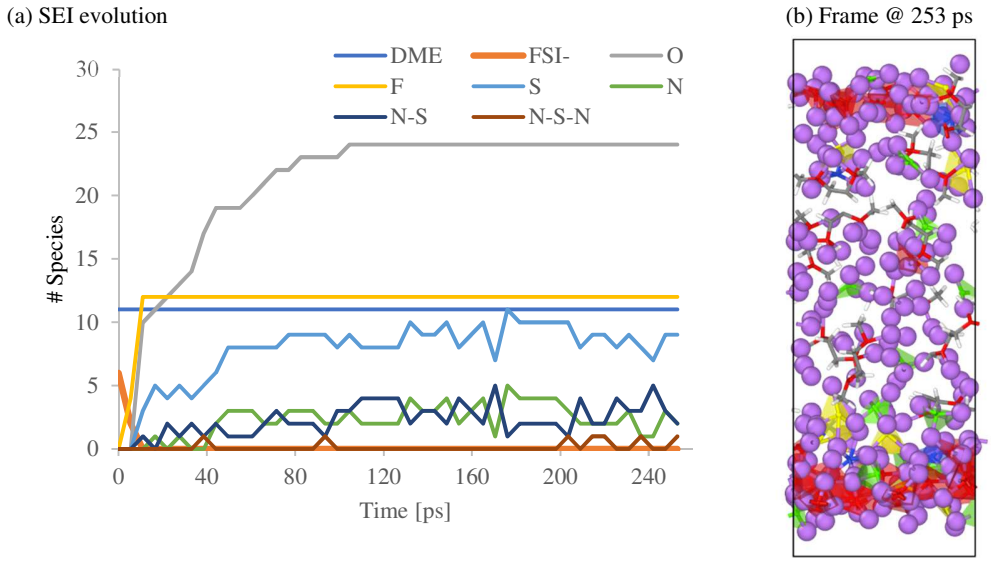

Figure 3: (a) SEI evolution with the 3.7 M E-2 electrolyte (Z_E/Z_A = 0.75), (b) final SEI configuration highlighting the inorganic SEI (polyhedral domains) and the DME-dissolved Li^+ ions. Atom colors as in Figure 1 and polyhedral coloring as in Figure 2.

Figure 4 shows the end frames of the SEIs derived from various electrolyte formulations based on LiFSI/DME and LiFSI/DMC. The histogram in Figure 5 summarizes the fraction of residual solvent and the relative content of LiO, LiS, LiN, LiH, and LiF in the inorganic SEI in terms of O/F, S/F, N/F, and H/F ratios. The 0.94 fraction of surviving DME molecules for the 1 M E-1 electrolyte case shows that nearly all solvent remain after the FSI^- anions decompose. Furthermore, the dispersed inorganic SEI formed from this E-1 electrolyte (SEI structure plotted in Figure 2(e)) has the oxygen to fluorine molar ratio (O/F) equal to 2.0, and the S/F and N/F ratios are both 1.0. These specific molar ratios are found in the molecular structure of the FSI^- anion and demonstrate that the inorganic SEI comes mainly from FSI^- anions. Finally, the 1.0 H/F molar ratio indicates the formation of lithium hydride, which is

experimentally reported in lithium metal anodes cycled in LiFSI/DME, LiFSI/DMC, and LiFSI/propylene carbonate (PC) electrolytes.[45] The DME solvent survives despite the increment in LiFSI concentration in the 3.7 M E-2 electrolyte; the O/F fraction remains equal to 2.0, but the S/F and N/F ratios lower to 0.75 and 0.16, which, together with S-N and N-S-N species present in Figure 3(a) indicates incomplete FSI^- reduction. The increase in $LiFSI^-$ concentration correlates with incomplete FSI^- decomposition, further confirmed below with calculations with LiFSI:DMC electrolytes.

No DMC molecule survives in the 0.91 M C-1 electrolyte. Instead, the oxygen released after the DMC decomposition leads to a dispersed SEI (Figure 4(a)) with a high O/F molar ratio equal to three. The 2.0 S/F molar ratio suggests complete FSI^- defluorination, but the N/F and H/F ratios are zero. The DMC decomposition produces a complex SEI structure quantified in the histogram plotted in Figure S1; The major species are $O\text{-}CH^-_3$ and CH_3^- radicals interacting with dissolved Li^+ ions via $O\text{-}Li^+$ and $C\text{-}Li^+$ interactions; and radical oligomers such as $OCCO^{4-}$, CO^{3-}, CCO^{2-}, and CN^-. The CN^- radical shows that nitrogen released from complete FSI- reduction also goes to the organic SEI phase. The dispersed inorganic SEI and the uncontrolled DMC reduction that leads to a massive presence of radical oligomers could lead to uncontrolled SEI growth to the detriment of the battery performance, in agreement with the low 50% Coulombic efficiency (CE) reported in Li^+ plating/stripping experiments performed with a lithium-metal battery with a 0.97 M LFSI/DMC electrolyte at a high current density (1 mA/cm^2) and capacity (1 mAh/cm^2).[43]

The 4.6 M C-2 electrolyte produces an extended, amorphous, inorganic SEI, as shown in Figure 4(b), mediated by a complex organic phase made from FSI^- and DMC decomposition products. The O/F ratio is two, the S/F ratio is 0.4, and the LiH phase becomes significant as the H/F increases to 0.6. This LiH phase comes from the DMC decomposition as no DMC molecule survives. The histogram in Figure S2 lists the species present in the SEI. The simultaneous decomposition of FSI^- anions and DMC molecules produces $S\text{-}N^{2-}$, $S\text{-}CH_2\text{-}O^-$, $C\text{-}C\text{-}S^{2-}$, and $O\text{-}CH_2\text{-}S\text{-}N\text{-}CH_2\text{-}O^{2-}$, among other radical oligomers. As with the

DME-based electrolytes, S-N bonding indicates incomplete FSI^- reduction associated with the increment of salt concentration.

We also studied two hypothetical supersaturated formulations, 10 M E-4 and 10 M C-3. The red polyhedra in Figure 4 (c) and (d) show compact and LiO-dominated inorganic phases with the O/F fractions equal to 1.81 and 2.37 for the E-4 DME- and C-3 DMC-based electrolytes, respectively. The 0.95 fraction of residual DME indicates that nearly all oxygen comes from FSI^- reduction. However, the low 1.81 O/F ratio suggests the oxygen species not only get spent in the inorganic SEI but also in the organic phase. Conversely, the high 2.37 O/F ratio for the C-3 DMC-based electrolyte is due to complete solvent decomposition. In the same way, the 0.44 and 0.42 S/F fractions in both cases, together with no structures with S-F bonding in the inorganic phases, as quantified in Figure S3, indicate a significant sulfur consumption in the organic phase. Furthermore, the 10 M C-3 SEI evidences the formation of lithium hydride (H/F = 0.37) from the DMC reduction.

Another aspect to highlight is the positive correlation of the inorganic SEI phase density with the LiFSI concentration. We isolated the inorganic SEI phases and calculated their densities after computing the surrounding van der Waals isosurfaces for each case using the MS built-in "Atom volumes & surfaces" tool.[40] The density of the LiFSI/DME-derived inorganic SEI phase increases from 0.98 to 1.23 g/cm^3 for the 3.7 M E-2 and 10 M E-4 formulations. Meanwhile, the LiFSI-DMC-derived phases also increase from 0.96 to 1.06 g/cm^3 for the 4.6 M C-2 and 10 C-3, respectively. Increased LiFSI concentration leads to more compact inorganic SEI phases where LiO and LiF oxides are dominant and segregated. Moreover, SEI swelling experiments with a modified thin-film vitrification method have shown a smaller swelling ratio in SEI layers derived from high concentrated 4 M LiFSI:DME electrolytes compared to 1 M LIFSI:DME.[18] This behavior correlates with calculations that show denser and more compact inorganic SEIs with increased LiFSI concentrations, which might indicate that inorganic-dominated SEIs are mechanically robust and could play a better passivating role during battery operation.

On the other side, our calculations show that supersaturated electrolytes lead to incomplete FSI-decomposition and formation of radical oligomers with the solvent reduction products. These results suggest a critical LiFSI concentration that optimizes the SEI structure, and further studies on this matter are underway and will be published soon. The DMC-derived inorganic phase is significantly more diverse than the LiFSI/DME electrolyte. Still, the absence of residual solvent in the organic SEI could limit Li^+ transport, trigger uncontrolled SEI growth, and eventually lead to the formation of "dry SEIs."[15]

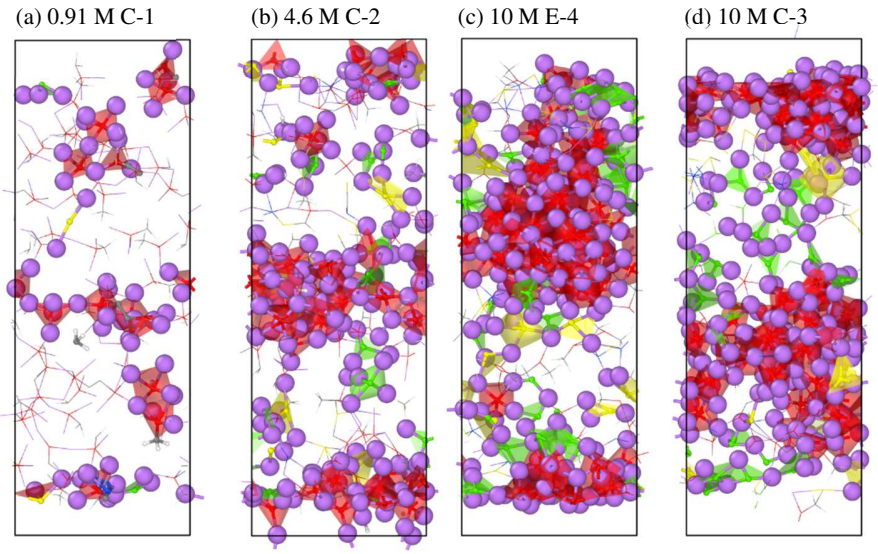

Figure 4: Final SEI configurations derived from four different electrolytes: (a) 0.91 M C-1, (b) 4.6 M C-2, (c) 10 M E-4, (d) 10 M C-3. The same electrolyte to anode ratio applies to all four calculations (ZE/ZA = 0.75). Atom colors as in Figure 1 and polyhedral coloring as in Figure 2.

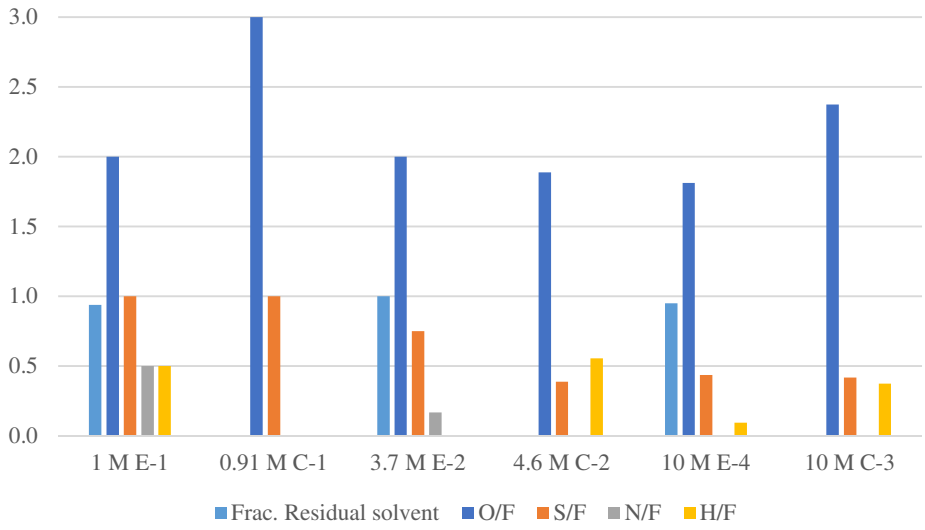

Figure 5: Fraction of residual solvent and relative LiO, LiS, LiN, LiH, and LiF content in terms of O/F, S/F, N/F, and H/F fractions in the inorganic SEI derived from six different electrolyte formulations: 1 M E-1, 0.91 M C-1, 3.7 M E-2, 4.6 M C-2, 10 M E-4, 10 M C-3. Z_E/Z_A = 0.75 in all cases.

Localized High Concentration Electrolytes

LHCE electrolytes show improved cycling stability compared to the equivalent HCE formulation and can potentially lower costs due to the lowered lithium salt consumption.[8, 42] Figure 6 summarizes the relative content of LiO, LiS, LiN, LiH, and LiF in the inorganic SEIs formed from the four LHCE formulations listed in Table 1, and Figure 7 shows the formed SEIs structures in each case. No FSI^- anions survive in either electrolyte formulation. Instead, all reduce to grow the inorganic SEI and form radical oligomers together with carbon species from reduced solvent and diluent molecules. The DME solvent survives in the 1.52 M ET-1 and 1.65 M EB-1 electrolytes, while all DMC molecules in the 1.35 CT-1 and 2.52 CB-1 electrolytes decompose. Regarding the residual diluent after the SEI formation, all TTE reduces irrespective of the solvent present. Conversely, 25 and 17 % of the initial BTFE survive in the 1.65 M EB-1 and 2.52 M CB-1 electrolytes. This higher BTFE resistance to reduction might correlate with earlier calculations from us that showed no BTFE in Li^+ solvation shells in LiFSI:DMC/TTE

electrolyte but Li^+-TTE interactions in LiFSI:DMC:TTE electrolytes. [33, 34] The Li^+-TTE interaction via Li^+-F coordination lowers the TTE LUMO levels and makes diluent more prone to reduction.

The O/F molar ratio in the inorganic SEI phase varies across the four electrolyte formulations. Still, it is significantly lower than the equivalent HCE electrolytes due to the increase in fluorine from the diluent decomposition. Figure 7 shows that the LiF phase is now dominant, which is significantly more evident in the LHCE formulations with TTE. This agrees with XPS measurements performed on a lithium metal anode cycled with a LiFSI:DME/TTE electrolyte (1:1.2:3 molar ratio), showing a significant increase in the F atomic ratio and a decrease in the C atomic ratios.[42] Even though our calculations are limited to the initial mass transfer processes forming these inorganic phases, comparing our calculations with these measurements performed on cycled lithium metal validates our results, at least qualitatively, on the existence of specific species determining the SEI morphology.

Another set of XPS results that agree with our observations comes from a Li||NCM622 battery with a LiFSI:DMC/TTE electrolyte (1:1.5:1.5), which shows a stronger LiF peak and a weaker S-F signal compared to the equivalent HCE LiFSI:DMC electrolyte.[43] Compared to the LiO phases in SEI structures derived from the equivalent HCE formulations 3.7 M E-2 and 4.4 M E-3, the LiF phase formed from the 1.52 M ET-1 electrolyte is significantly more dispersed. This change in the LiO and LiF content and the degree of dispersion of the inorganic SEI might correlate with improved > 99.3% CE efficiency measured in an LMB battery cycled with a LiFSI:DME/TTE electrolyte (1:1.2:3 molar ratio) compared to the 99.1 % efficiency with the equivalent LiFSI:DME HCE electrolyte.[42] The nonzero N/F ratios in the histogram in Figure 6 for the inorganic SE derived from the electrolytes 1.65 M EB-1, 1.35 M CT-1, and 2.52 M CB-1 indicates the presence of LiN in the inorganic SEI, in agreement with the nitride signal (Li_xN, 396 eV, N 1s) detected on lithium metal anodes cycled with a LiFSI:DME/TTE electrolyte (1:1.2:3 molar ratio).[46] This LiN phase suggests a complete reduction of some FSI^- anions. However, the histograms in Figure S4 show the presence of N-S-N, N-S, C-C-S-N, CH_2-CS-CH-S, and S-S-CH-C-CH_2,

among other structures, which evidence incomplete FSI^- decomposition and formation of complex oligomer structures together with solvent decomposition products across all LHCE formulations studied.

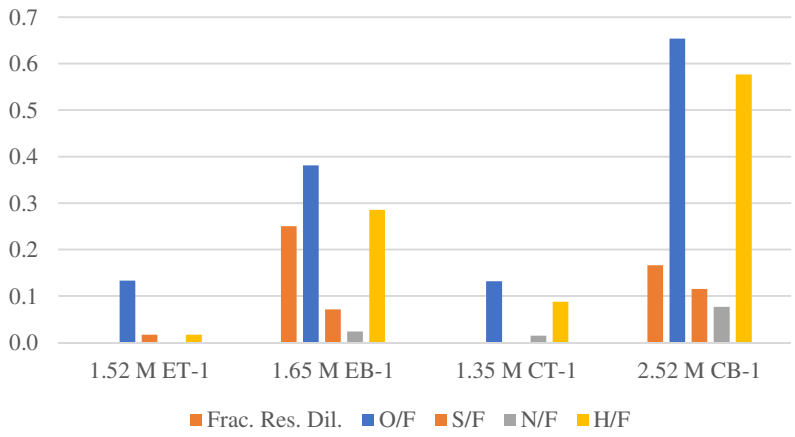

Figure 6: Fraction of residual solvent and relative content of LiO, LiS, LiN, LiH, and LiF in terms of O/F, S/F, N/F, and H/F fractions in the inorganic SEI derived from four LHCE electrolytes: 1.57 M ET-1, 1.65 M EB-1, 1.35 M CT-1, and 2.52 M CB-1. SeeTable 1 for references to these electrolyte labels.

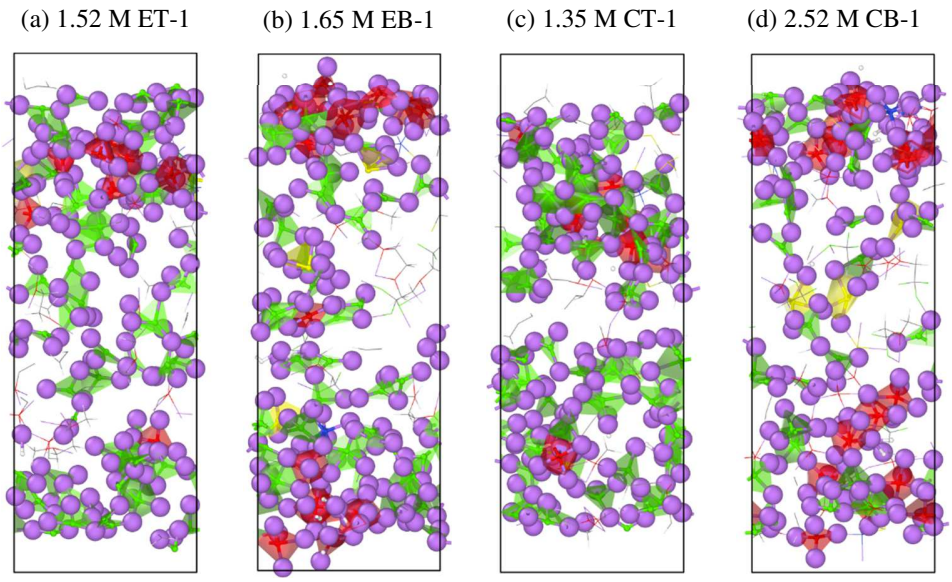

Figure 7: SEI structures from after four different LHCE electrolytes: 1.52 M ET-1 , 1.65 M EB-1, 1.35 M CT-1, and 2.52 M CB-1. Z_E/Z_A = 0.75 across all calculations. Atom colors as in Figure 1 and polyhedral coloring as in Figure 2.

Tuning the Electrolyte-to-Anode Ratio

The experimental data suggest that LMBs batteries always show a sudden capacity drop after repeated cycling and eventually fail regardless of the electrolyte formulation.[15, 16] However, the electrolyte formulation and even the electrolyte-to-anode ratio significantly impact the SEI degradation mechanisms and balance the rates of lithium consumption and electrolyte depletion to extend the battery life to meet the minimum operational needs. Our results show that LIFSI:DME electrolytes produce a dense and compact inorganic SEI with low solvent decomposition, potentially improving the battery performance. Figure S5 shows three initial configurations packed with a 4.4 M E-3 electrolyte at three different electrolyte-to-anode ratios corresponding to a case with a minimum amount of electrolyte ($Z_E/Z_A = 0.36$), an intermediate ratio ($Z_E/Z_A = 0.75$), and an excess amount of electrolyte ($Z_E/Z_A = 2.79$). Figure 8 (a) to (c) show the corresponding SEIs structures, and Figure 8 (d) shows the molar ratios O/F, S/F, and N/F that account for the changes in the relative content of LiO, LiS, LiN, and LiF in the inorganic phase. As in our simulations above, the DME solvent is highly stable, and all molecules survive in these three cases.

The assembly with a minimum amount of electrolyte (Figure 8 (a)) shows some residual lithium metal covered by a first inorganic inner layer followed by Li^+ ions dissolved in the DME electrolyte and an outer and compact inorganic SEI film. The inorganic SEI shows a LiO phase dominant (red polyhedral network) surrounded by LiS, LiN, and LiF clusters with molar ratios O/F, S/F and N/F equal to 2.0, 0.9, and 0.4, and an $S\text{-}N^{3-}$ radical. Similar heterogenous SEI structures have been reported with in situ electrochemical atomic force microscope (AFM) on graphite electrodes.[47, 48] The intermediate case (Figure 8b) has no lithium metal left but still shows a layered SEI with a compact inorganic phase surrounded by dissolved Li^+ ions. The higher electrolyte content leads to the formation of more $S\text{-}N^{3-}$ structures compared to the first case, which indicates a less efficient FSI^- reduction.

Finally, in Figure 8c, the calculation with an excess amount of electrolyte ($Z_E/Z_A = 2.79$) produces dispersed LiO and LiF clusters at an O/F ratio equal to 0.72, surrounded by dissolved Li^+ ions and DME molecules. The histogram in Figure S6 shows a heterogeneous SEI phase with multiple and complex

radical oligomers such as O-S-N-SO_2^{3-}, SO_2-N-SO_2^{3-}, and O-S-N-S-O^-, among others, that indicate incomplete FSI^- reduction. These changes in the electrolyte-to-anode ratio significantly impact the SEI structure and suggest the existence of an optimal ratio that can potentially balance the rate of electrolyte depletion and lithium consumption. This observation is also pointed out in experiments with Li‖$LiNi_{0.6}Mn_{0.2}Co_{0.2}O_2$ batteries cycled with multiple anode-to-catio capacity ratios. A 20 µm thin lithium metal anode with a negative to positive areal capacity (N/P ratio) equal to 1 produced a thin and uniform "wet SEI" film that minimized cell polarization and extended the cell cycle life compared to other assembles with N/P ratios of 0 (Li-free anode), and >2.5 (thick Li pouch cells).[15]

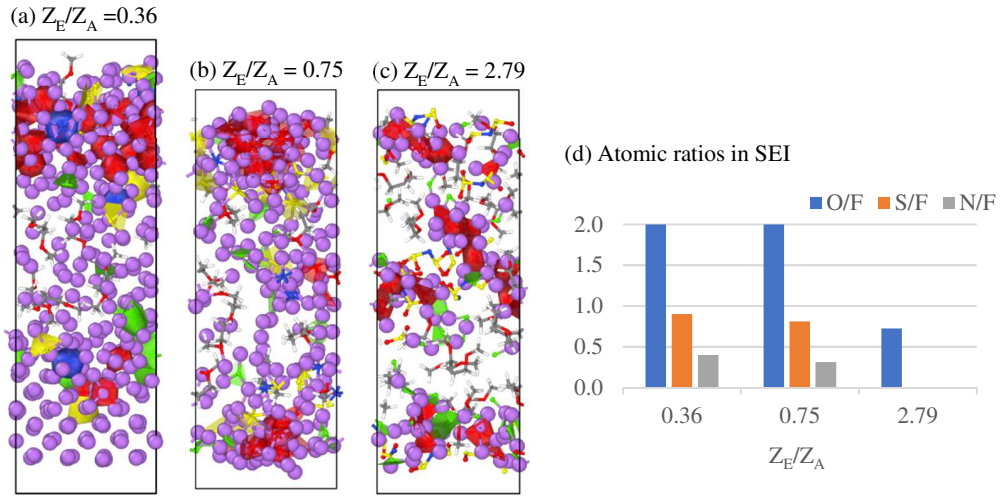

Figure 8: SEI structures from a 4.4 M E-3 electrolyte packed at three different electrolyte-to-anode (Z_E/Z_A) ratios (a) 0.36, (b) 0.75, and (c) 2.79; (d) relative LiO, LiS, LiN, and LiF content in terms of O/F, S/F/ and O/F ratios in the inorganic SEI phase. Atom colors as in Figure 1 and polyhedral coloring as in Figure 2.

Conclusions

We provide an atomic-level perspective of the SEI formation mechanisms and Li^+ dissolution with different electrolyte formulations and electrolyte-to-anode ratios. This work significantly improves the understanding of the SEI morphology and composition that correlates with experimental evidence from multiple sources. We describe the LiFSI reduction mechanism and find its dependence on the

concentration in the electrolyte formulations and type of solvent. The low concentration electrolytes grow a dispersed inorganic SEI phase surrounded by dissolved Li^+ ions.The ether DME solvent is highly stable, helps dissolve Li^+ ions and leads to the formation of a heterogeneous "wet-SEI" structure. The carbonate DMC solvent reduces in all cases studied and reacts with FSI^- reduction products to growth complex SEI morphologies that resemble a "dry-SEI" that might be highly unstable and lead to uncontrolled electrolyte decomposition. The dry SEI composition depends on the LiFSI concentration and on the presence of diluents. HCE electrolytes grow compact and continuous LiO domains surrounded by LiF, LiN, and LiF clusters; the higher the LiFSI concentration, the denser these inorganic domains are. On the other side, the LiF phase becomes dominant with LHCE electrolytes; the diluent decomposition increases the availability of fluorine species. Moreover, the TTE diluent is more reactive than BTFE.

Our study further reveals that the SEI morphology is highly dependent on the electrolyte-to-anode ratio; the FSI^- decomposition becomes less effective with higher electrolyte-to-anode ratios, leading to the formation of complex sulfurized radical oligomers that might hinder the SEI integrity. We suggest the existence of a critical LiFSI concentration and electrolyte-to-anode ratio that optimizes the SEI structure by balancing the rate of electrolyte depletion and lithium consumption.

Experiments have shown that there are changes in the Coulombic efficiency and cell capacity during cycling; this has been attributed to a series of factors including the SEI continuous change during cycling. Our study aims to narrow down this gap in understanding the SEI dynamics, at least at the initial stages of formation. Future work in progress using coarse grained methods will use the information reported in this work to address longer time scales and the influence of the SEI dynamics on cycling and plating/stripping events.

Acknowledgements

This work was supported by the Assistant Secretary for Energy Efficiency and Renewable Energy, Office of Vehicle Technologies of the US Department of Energy through the Advanced Battery Materials

Research (BMR) Program (Battery500 Consortium phase 2) under DOE contract No. DE-AC05-76RL01830 from the Pacific Northwest National Laboratory (PNNL). Computational resources from the Texas A&M University High Performance Research Computing are gratefully acknowledged.

References

[1] X.-B. Cheng, R. Zhang, C.-Z. Zhao, F. Wei, J.-G. Zhang, Q. Zhang, Adv. Sci, 3 (2016) 1500213.

[2] J.-S. Kim, T.H. Hwang, B.G. Kim, J. Min, J.W. Choi, Adv. Funct. Mater., 24 (2014) 5359-5367.

[3] T. Kim, W. Song, D.-Y. Son, L.K. Ono, Y. Qi, J. Mater. Chem. A, 7 (2019) 2942-2964.

[4] J. Liu, Z. Bao, Y. Cui, E.J. Dufek, J.B. Goodenough, P. Khalifah, Q. Li, B.Y. Liaw, P. Liu, A. Manthiram, Nat. Energy, (2019) 1.

[5] S.R. Sivakkumar, A.S. Milev, A.G. Pandolfo, Electrochim. Acta, 56 (2011) 9700-9706.

[6] L. Chen, X. Fan, X. Ji, J. Chen, S. Hou, C. Wang, Joule, 3 (2019) 732-744.

[7] Q. Wang, B. Liu, Y. Shen, J. Wu, Z. Zhao, C. Zhong, W. Hu, Adv. Sci, 8 (2021) 2101111.

[8] S. Chen, J. Zheng, D. Mei, K.S. Han, M.H. Engelhard, W. Zhao, W. Xu, J. Liu, J.-G. Zhang, Adv. Mater., 30 (2018) 1706102.

[9] Y. Gao, Z. Yan, J.L. Gray, X. He, D. Wang, T. Chen, Q. Huang, Y.C. Li, H. Wang, S.H. Kim, T.E. Mallouk, D. Wang, Nat. Mater., 18 (2019) 384-389.

[10] D. Lin, Y. Liu, Z. Liang, H.-W. Lee, J. Sun, H. Wang, K. Yan, J. Xie, Y. Cui, Nat. Nanotechnol, 11 (2016) 626-632.

[11] Z. Cao, B. Li, S. Yang, Adv. Mater., 31 (2019) 1901310.

[12] X. Shen, R. Zhang, P. Shi, X. Chen, Q. Zhang, Adv. Energy Mater., 11 (2021) 2003416.

[13] B. Liu, J.-G. Zhang, W. Xu, Joule, 2 (2018) 833-845.

[14] G.M. Hobold, J. Lopez, R. Guo, N. Minafra, A. Banerjee, Y. Shirley Meng, Y. Shao-Horn, B.M. Gallant, Nat. Energy, 6 (2021) 951-960.

[15] C. Niu, D. Liu, J.A. Lochala, C.S. Anderson, X. Cao, M.E. Gross, W. Xu, J.-G. Zhang, M.S. Whittingham, J. Xiao, J. Liu, Nat. Energy, 6 (2021) 723-732.

[16] C. Niu, H. Lee, S. Chen, Q. Li, J. Du, W. Xu, J.-G. Zhang, M.S. Whittingham, J. Xiao, J. Liu, Nat. Energy, 4 (2019) 551-559.

[17] Y. Zhu, V. Pande, L. Li, B. Wen, S. Pan Menghsuan, D. Wang, Z.-F. Ma, V. Viswanathan, Y.-M. Chiang, Proc. Natl. Acad. Sci. U. S. A, 117 (2020) 27195-27203.

[18] Z. Zhang, Y. Li, R. Xu, W. Zhou, Y. Li, T. Oyakhire Solomon, Y. Wu, J. Xu, H. Wang, Z. Yu, T. Boyle David, W. Huang, Y. Ye, H. Chen, J. Wan, Z. Bao, W. Chiu, Y. Cui, Science, 375 (2022) 66-70.

[19] E. Peled, J. Electrochem. Soc., 126 (1979) 2047-2051.

[20] Y. Liu, P. Yu, Y. Wu, H. Yang, M. Xie, L. Huai, W.A. Goddard, T. Cheng, J. Phys. Chem. Lett., 12 (2021) 1300-1306.

[21] Y. Liu, Q. Sun, P. Yu, Y. Wu, L. Xu, H. Yang, M. Xie, T. Cheng, W.A. Goddard, J. Phys. Chem. Lett., 12 (2021) 2922-2929.

[22] Y. Liu, Q. Sun, P. Yu, B. Ma, H. Yang, J. Zhang, M. Xie, T. Cheng, J. Mater. Chem. A, 10 (2022) 632-639.

[23] G. Kresse, J. Furthmüller, Phys. Rev. B, 54 (1996) 11169-11186.

[24] G. Kresse, J. Furthmüller, Comput. Mater. Sci., 6 (1996) 15-50.

[25] G. Kresse, J. Hafner, Phys. Rev. B, 47 (1993) 558-561.

[26] G. Kresse, J. Hafner, Phys. Rev. B, 49 (1994) 14251-14269.

[27] G. Kresse, D. Joubert, Phys. Rev. B, 59 (1999) 1758-1775.

[28] J.P. Perdew, K. Burke, M. Ernzerhof, Phys. Rev. Lett., 77 (1996) 3865-3868.

[29] H.J. Monkhorst, J.D. Pack, Phys. Rev. B, 13 (1976) 5188-5192.

[30] E.P. Kamphaus, P.B. Balbuena, J. Phys. Chem. C, 121 (2017) 21105-21117.

[31] S. Plimpton, J. Comput. Phys., 117 (1995) 1-19.

[32] Y. Yamada, A. Yamada, J. Electrochem. Soc., 162 (2015) A2406-A2423.

[33] S. Perez-Beltran, X. Cao, J.-G. Zhang, P.Z. El-Khoury, P.B. Balbuena, J. Mater. Chem. A, 9 (2021) 17459-17473.

[34] S. Perez Beltran, X. Cao, J.-G. Zhang, P.B. Balbuena, Chem. Mater., 32 (2020) 5973–5984.

[35] M. Otani, O. Sugino, Phys. Rev. B, 73 (2006) 115407.

[36] J. Haruyama, T. Ikeshoji, M. Otani, J. Phys. Chem. C, 122 (2018) 9804-9810.

[37] K. Leung, S.B. Rempe, M.E. Foster, Y. Ma, J.M. Martinez del la Hoz, N. Sai, P.B. Balbuena, J. Electrochem. Soc., 161 (2013) A213-A221.

[38] L.E. Camacho-Forero, T.W. Smith, S. Bertolini, P.B. Balbuena, J. Phys. Chem. C, 119 (2015) 26828-26839.

[39] K. Doll, N. Harrison, V. Saunders, J. Phys.: Condens. Matter, 11 (1999) 5007.

[40] D.S. BIOVIA, San Diego: Dassault Systemes, (2014).

[41] H. Zhang, C. Shen, Y. Huang, Z. Liu, Appl. Surf. Sci., 537 (2021) 147983.

[42] X. Ren, L. Zou, X. Cao, M.H. Engelhard, W. Liu, S.D. Burton, H. Lee, C. Niu, B.E. Matthews, Z. Zhu, C. Wang, B.W. Arey, J. Xiao, J. Liu, J.-G. Zhang, W. Xu, Joule, 3 (2019) 1662-1676.

[43] N. Piao, X. Ji, H. Xu, X. Fan, L. Chen, S. Liu, M.N. Garaga, S.G. Greenbaum, L. Wang, C. Wang, X. He, Adv. Energy Mater., 10 (2020) 1903568.

[44] X. Cao, P. Gao, X. Ren, L. Zou, H. Engelhard Mark, E. Matthews Bethany, J. Hu, C. Niu, D. Liu, W. Arey Bruce, C. Wang, J. Xiao, J. Liu, W. Xu, J.-G. Zhang, Proc. Natl. Acad. Sci. U. S. A, 118 (2021) e2020357118.

[45] Z. Shadike, H. Lee, O. Borodin, X. Cao, X. Fan, X. Wang, R. Lin, S.-M. Bak, S. Ghose, K. Xu, C. Wang, J. Liu, J. Xiao, X.-Q. Yang, E. Hu, Nat. Nanotechnol, 16 (2021) 549-554.

[46] Q. Wu, X. Tang, Y. Qian, J. Duan, R. Wang, J. Teng, J. Li, ACS Appl. Energy Mater, 4 (2021) 10234-10243.

[47] A.v. Cresce, S.M. Russell, D.R. Baker, K.J. Gaskell, K. Xu, Nano Lett., 14 (2014) 1405-1412.

[48] A. Wang, S. Kadam, H. Li, S. Shi, Y. Qi, npj Comput. Mater., 4 (2018) 15.